Journal Pre-proof

Age-hardening behavior, corrosion mechanisms, and passive film structure of nanocrystalline Al-V supersaturated solid solution

J. Christudasjustus , M.R. Felde , C.S. Witharamage , J. Esquivel , A.A. Darwish , C. Winkler , R.K. Gupta

PII: S1005-0302(22)00591-6
DOI: https://doi.org/10.1016/j.jmst.2022.06.044
Reference: JMST 4149

To appear in: *Journal of Materials Science & Technology*

Received date: 21 March 2022
Revised date: 17 June 2022
Accepted date: 18 June 2022

Please cite this article as: J. Christudasjustus , M.R. Felde , C.S. Witharamage , J. Esquivel , A.A. Darwish , C. Winkler , R.K. Gupta , Age-hardening behavior, corrosion mechanisms, and passive film structure of nanocrystalline Al-V supersaturated solid solution, *Journal of Materials Science & Technology* (2022), doi: https://doi.org/10.1016/j.jmst.2022.06.044

Highlights

- Synthesis of a nanocrystalline Al-5at.%V alloy with high solid solubility of V by high-energy ball milling
- Study on the age hardening behavior of the ball milled Al-V alloy
- Corrosion behavior as a function of age hardening time and temperature
- Study of the passive film and pits using transmission electron microscope
- Microstructural features causing passive film breakdown and subsequent pit growth or repassivation

Age-hardening behavior, corrosion mechanisms, and passive film structure of nanocrystalline Al-V supersaturated solid solution

J. Christudasjustus [a], M. R. Felde [b], C.S. Witharamage [a], J. Esquivel [b], A.A. Darwish [a], C. Winkler [a], R.K. Gupta [a, *]

[a] Department of Materials Science and Engineering, North Carolina State University, Raleigh, NC 27606, United States of America

[b] Department of Chemical, Biomolecular and Corrosion Engineering, The University of Akron, Akron, OH 44325, United States of America

*Corresponding author.

E-mail address: rkgupta2@ncsu.edu (R.K. Gupta).

Abstract: The effect of age-hardening on microstructure, hardness, and corrosion of an Al-5at.%V alloy, produced using high-energy ball milling and subsequent cold compaction, has been investigated. The alloy exhibited a grain size below 100 nm and extremely high solid solubility of V in Al (3.1 at.%). The age-hardening was carried out at 150, 200, and 250 ℃. The peak-aged condition of 150 ℃ demonstrated the highest hardness—transpired from grain refinement, precipitation, and solid solution hardening. The corrosion resistance of the Al-5at.%V alloy was studied as a function of aging conditions. The peak-aged condition retained the corrosion resistance while it deteriorated in the over-aged condition. Nonetheless, the corrosion resistance of the ball-milled Al alloys in all the aging conditions was superior to that of pure Al. The passive film structure and origin of corrosion were studied using scanning/transmission electron microscopy (S/TEM). The high corrosion resistance of the alloy was attributed to the V enrichment at the film/metal interface and deposition of V on the cathodic phases, which suppresses the dissolution of Al within the pit and therefore promotes repassivation in the early stages of corrosion.

Keywords: Al alloys; Nanocrystalline alloy; Age-hardening; Ball milling; Corrosion; Hardness

1. Introduction

Improving the strength of aluminum alloys has been of interest due to their lightweight and use in aerospace and automotive applications [1–4]. Heat-treatable Al alloys such as 2xxx series alloys are used in aircrafts and truck bodies in riveted construction, and 7xxx series alloys are used for aircraft wing structures [5]. These alloys exhibit complex microstructure which includes various secondary phases such as precipitates, constituent particles, and dispersoids. These secondary phases render electrochemical heterogeneity within the microstructure and stimulate detrimental corrosion by promoting localized galvanic interactions [6–8]. The extent of localized corrosion by the secondary phases

depends on their chemical composition, volume fraction, shape, size, and distribution. A high-volume fraction of the precipitates is required for strength in precipitation-hardened alloys, which causes poor corrosion resistance.

Recently, nanocrystalline Al alloys produced by high-energy ball milling (HEBM) have been reported to exhibit high strength along with high corrosion resistance [4, 9–13]. The high solid solubility of the alloying elements resulted in high pitting potential and repassivation potential. The detrimental effect of any secondary phases was subdued by the high solid solubility of alloying elements in matrix [4, 14, 15]. The solid solubility of the alloying elements was far from the equilibrium—several orders of magnitude higher than the solubility predicted by the phase diagrams [9, 16]. The alloys exhibited good thermal stability [17, 18]. Therefore, these alloys could respond to the precipitation hardening. However, the age-hardening behavior and subsequent corrosion resistance of these ball-milled Al alloys have not been reported in the literature. Investigating the effect of age-hardening on microstructure and corrosion resistance is of great merit since ball-milled alloys are not in an equilibrium state. If the adequate activation energy is provided, they will tend to decompose to stable phases and result in grain growth [4, 19, 20]. Literatures have reported various routes to suppress grain growth kinetics at elevated temperature, which involves and is not limited to introducing secondary phase particles at the grain boundaries. Secondary phase particles such as NbB_2, VB_2, and TiB_2 were used as grain refiners during casting, which provided an additional advantage in reducing porosity and hot tearing [21–23]. However, preserving the nanocrystalline structure exhibiting supersaturated solid solution, requires an alternate route to retain the corrosion resistance while enhancing the mechanical properties. Grain size, solid solubility, and precipitation in such alloys can be controlled by alloying the appropriate solute element. Among various alloying elements, e.g., molybdenum, vanadium, nickel, niobium, chromium, silicon, titanium, and manganese that help in achieving high-

strength and high corrosion resistance [10, 16, 24], vanadium offers high thermal stability, high corrosion resistance, and high strength [9, 18, 25]. V also has a low diffusion coefficient in Al (4.85×10^{-24} m^2/s at 400 ℃ [26]), which is expected to retard the decomposition of solid solution as well as coarsening of the precipitates and offers flexibility in controlling the microstructure and properties [26].

The oxide film formed on passive metals such as Al is the primary barrier to corrosion [27]. The passive film in the Al alloys is compromised in halide-containing environments, which causes pitting corrosion. Alloying with corrosion-resistant elements (such as Cr, Mo, and Ti) using non-equilibrium processing techniques such as sputtering is reported to result in alloys with high corrosion resistance [28–34]. These alloys were single-phase solid solutions and therefore exhibited a uniform microstructure. On the contrary, the ball-milled Al alloys, showing high corrosion resistance, are heterogeneous and comprised of solute-rich matrix and secondary phases in the form of precipitates and/or unalloyed alloying elements [10, 35]. Understanding corrosion mechanisms of such heterogeneous microstructure are challenging, and several plausible mechanisms have been proposed: 1) solute enrichment at the passive film/metal interface that can act as a barrier layer and enhance the oxide film from breakdown, 2) release of oxyanion species like molybdates and vanadates that can inhibit corrosion in the initial stage of corrosion and promote repassivation, 3) doping of passive film with solute ions to annihilate point defects, and 4) deposition of solute ions over cathodic particles to retard the cathodic reaction leading to slower pit growth or repassivation. The evidence for these proposed mechanisms in HEBM Al alloys is not reported extensively. Age-hardening enables controlled decomposition of the matrix to create microstructure with a wide range of precipitate size and distribution along with varying matrix composition and thus offers to study the role of microstructure on corrosion. The corrosion of Al alloys is influenced by the surface film. However, the challenge lies in investigating the effect of

microstructural features on the formation and breakdown of the surface film [36, 37]. Most of the studies on characterizing the surface film are based on X-ray photoelectron spectroscopy and secondary ion mass spectrometry which lack the lateral resolution to resolve the effects of fine precipitates. This study presents the use of scanning/transmission electron microscopy (S/TEM) in studying the surface film, pit initiation, and subsequent inhibition of the pit growth. The supersaturated nanocrystalline structure in this work is produced using the HEBM. The influence of age-hardening on microstructure, hardness, and strengthening mechanisms is also presented.

2. Experimental Procedure

2.1. Powder preparation and consolidation

Aluminum powder (99.7% purity) with mesh size –50/+100 and 5 at.% vanadium powder (99.8% purity) with mesh size ~100 were milled using a high-energy ball mill (HEBM) in the controlled argon atmosphere to avoid the oxidation reaction. The milling was done at 280 r/min for 100 h with a pause of 30 min after every 1 h. Stearic acid of 1.5 wt.% was used as a process controlling agent (PCA) to avoid agglomeration and cold welding of powder. Hardened stainless-steel balls with 10 mm diameters having a ball to powder ratio of 16:1 were used inside the hardened stainless-steel vials. The produced powder was then cold compacted at 3 GPa for 10 min to obtain a 7 mm diameter with 3 mm thick samples.

2.2. Heat treatment and hardness

The cold compacted samples were ground to 1200 grit and then were heat-treated in an oven and compared for three different temperatures: 1) 150 ℃, 2) 200 ℃, and 3) 250 ℃. This aging temperature range was chosen based on better control over precipitate formation and distribution. In the rest of the work, under-aged, peak-aged, and over-aged conditions will be denoted as UA, PA, and OA, respectively. Vickers micro-hardness test was conducted

to obtain the change in hardness with respect to age time and temperature using an applied load of 50 g, and the average value of 10 readings was noted.

2.3. Microstructural characterization

Milled powders after the HEBM process and consolidated specimens were studied using scanning electron microscopy (SEM). The specimens were polished to a 0.05-micron surface finish using monocrystalline diamond suspension and ultrasonicated for 5 min to remove any contamination. Energy-dispersive X-ray spectroscopy (EDS) was performed to confirm the elemental distribution within the matrix. Additionally, an X-ray diffractometer (XRD) was performed on these specimens to identify intermetallic and solid solubility changes after the aging process. Cu-$K\alpha$ radiation (λ = 0.15406 nm) was used for 15°–85° 2θ range with a scan rate of 1°/min and step size of 0.02°. High-resolution XRD scans were performed at 0.0012° step size and a scanning rate of 0.08°/min between 39.6° and 41° 2θ.

S/TEM characterization of selected age-hardened specimens was conducted using Thermo Fisher Talos F200X to investigate the microstructural changes due to heat treatment and post-corrosion. Four age-hardened specimens, namely 150 ℃-PA, 150 ℃-OA, 250 ℃-PA, and 250 ℃-OA, were analyzed and compared to the base alloy. Moreover, two specimens, namely 250 ℃-PA and 250 ℃-OA were immersed in 0.1 M NaCl solution for two hours, followed by rinsing with deionized water to remove the NaCl residue and stored under an inert argon atmosphere for S/TEM characterization, which was crucial for correlating the pit initiation to the microstructural evolution. The S/TEM specimens were prepared by the FIB lift-out technique using a Thermo Fisher Quanta 3D FEG. An initial 300 nm layer of Pt was deposited via the electron beam on the interested region, followed by a 500 nm layer of Pt deposited with the ion beam to protect the surface from FIB-induced ion irradiation and implantation. The microstructure and surface modification were studied using two imaging modes: Bright field (BF) STEM—sensitive to phase-contrast from structural and

chemical change, and high angle annular dark-field (HAADF) STEM—sensitive to Z-contrast from atomic number.

2.4. Electrochemical tests

The specimens were mounted on epoxy and ground to 1200 grit using SiC papers, followed by ultrasonic cleaning for 10 min. The surface of 0.178 cm^2 was exposed for testing by covering the surrounding using polyester tape. The test was performed in a standard flat cell with a platinum wire mesh as the counter electrode. A saturated calomel electrode (SCE) was used as the reference. The specimens were immersed for 30 min in 0.01 M NaCl for open circuit potential (OCP) stabilization before the potentiodynamic polarization (PDP) test. The PDP test was carried out using Bio-Logic VMP300 potentiostat with the help of EC-Lab software. Anodic polarization was conducted from 50 mV_{SCE} below OCP towards the noble direction with the sweep rate of 0.167 mV/s until the current density reached 200 $\mu A/cm^2$ as described in [38].

3. Results

3.1. Ball-milled powder and initial microstructure after HEBM

Fig. 1(a) shows the backscattered electron (BSE) images of ball-milled powder from HEBM. The size of the powder was in the range of 5–70 μm with an average size of 32 μm. The ball-milled powder was cold compacted and was termed as base alloy herein. BSE image presented in Fig. 1(b) reveals uniform vanadium distribution in the matrix of the base alloy. Bright particles are observed in the matrix and confirmed to be Fe-rich particles, as shown in the inset of Fig. 1(b). The Fe-rich particles are commonly observed in ball-milled materials, originating from the abrasion of milling media, having a size range of 500 nm–1 μm [9]. The S/TEM-HAADF image of the base alloy (Fig. 1(c)) reveals the matrix to be heterogeneous at the nanoscale and contains three uniformly distributed phases—1) matrix, 2) a dark phase

denoted by the yellow arrow, and 3) fine bright particles with a size of 1.6 nm, shown by the white arrow. The EDS analysis revealed the dark phase to be carbon-rich, originating from the stearic acid, added as a process controlling agent. The bright phase is a V-rich phase, attributed to either unalloyed V or Al-V intermetallics formed along with the supersaturated solid solution during HEBM. Fig. 1(d) shows the TEM micrograph of grain distribution with the selected area electron diffraction (SAED) pattern as inset, and the speckled bright rings in the SAED pattern confirmed the formation of nano-sized grains after HEBM and exhibited crystallinity. The Al bright rings are indexed by yellow arrow and text, which showed the grain orientations of (111), (200), (220), (311), and (222) in the matrix and are typically observed in nanocrystalline FCC Al. Further, the grain size was estimated using the dark field (DF) images taken at (111) grain orientation from the (SAED) pattern. The statistical grain size analysis showed grains in the range of 10–70 nm with an average grain size of 29 nm.

3.2. Age-hardening behavior

The age-hardening curves of Al-5at.%V alloy at 150, 200, and 250 °C for different aging times are shown in Fig. 2. The hardness of Al-5at.%V base alloy exhibited 299 ± 8 HV. The peak hardness was dependent on the temperature, and the highest peak hardness was achieved for the lowest age-hardening temperature, i.e., 150 °C. The age-hardening kinetics appears to increase with the aging temperature. Hardness significantly increased in the first one hour of aging at 150 °C, followed by a sluggish increase up to 48 h, afterward leaping at the peak value of 344 ± 5 HV by 7 days (168 h) and dropped gradually with continued aging. A similar trend was observed for aging at 200 °C, and the peak hardness (340 ± 7 HV) was reached in 9 h. The hardness value for aging at 250 °C increased rapidly till 45 min of aging and dropped significantly after achieving the peak hardness of 336 ± 7 HV. Specimens for detailed microstructural studies were selected based on the age-hardening curves (Fig. 2), where three conditions were selected, i.e., under-aged (UA), peak-aged (PA), and over-aged

(OA) for each temperature. Notations for selected aging temperatures and conditions, along with the aging time, are provided in Table 1.

3.3. Microstructural evolution

The X-ray diffraction profiles of selected age-hardened alloys are presented in Fig. 3. The XRD profiles of the alloy aged at 150 and 200 ℃ show only Al peaks (Fig. 3(a, b)), whereas a diffraction peak corresponding to Al_3V at 40.06° is observed in the alloy over-aged at 250 ℃ (Fig. 3(c)). High-resolution XRD scans are presented in Fig. 3(d), confirming the presence of Al_3V in the alloy over-aged at 200 and 250 ℃, whereas it was not detected in the alloy over-aged at 150 ℃. The Fe-rich particles observed in SEM images were not revealed through XRD, indicating the content of Fe-rich particles to be below the detection limit of XRD.

High-energy ball mill technique is known to provide a supersaturated solid solution, and age-hardening is expected to result in the loss of solid solution along with precipitation. The change in solid solubility is obtained by measuring the lattice parameter of the matrix from XRD peak positions. Table 2 shows the values of lattice parameters for aged alloys. The solid solubility (SS) of V in Al at different aging conditions was calculated using the following equation [10] and shown in Fig. 4(a),

$$\mathrm{SS} = \frac{a_A - a_0}{m_x} \quad (1)$$

where a_A is the lattice parameter of Al-V alloy, a_o is the lattice parameter of pure Al (a_o = 0.40496 nm [39]), and m_x is the slope obtained from SS vs ($a_A - a_o$); here, m_x = –0.007909 nm/at.% [40]. At room temperature, the equilibrium solid solubility of V in Al is 5.43×10^{-7} at.% [18]. The base alloy exhibited solid solubility of V up to 3.1 at.% in Al which is 5.7×10^6 times higher than the equilibrium value. The solid solubility appears to decrease with

aging, which is attributed to the decomposition of Al-V solid solution to thermodynamic equilibrium phase—Al_3V. The decrease in solid solubility was dependent on both aging time and temperature. Higher aging time results in a rapid decrease in solid solubility. Over-aged alloy at 250 ℃ shows a solid solubility of 1.9 at.% V, which is significantly lower than that of the base alloy (3.1 at.%) yet six orders of magnitude higher than the equilibrium solid solubility of V in Al.

The average grain size shown in Fig. 4(b) was estimated from XRD data using the Scherrer method [41]. The grain growth was not significant and was dependent on aging time and temperature. Grain size remained below 40 nm for all the aging conditions. The grain size was also calculated using S/TEM analysis for selected specimens, as shown in Fig. 5(a–d). The BF, DF, and SAED pattern for the specimens are provided in supplementary data section S1. The specimens exhibited a grain size range of 10–100 nm with an average grain size below 50 nm except for 250 ℃-OA, which showed an average grain size of 68 nm. The average grain size estimated from XRD and S/TEM is in good agreement. The difference observed in the average grain size calculation between the two techniques can be attributed to the possible heterogeneous distribution of grain size and also the inability of XRD methods in accounting for the peak broadening due to dislocations and sub-grains. The S/TEM study in this work is restricted to a 5 μm × 7 μm area analysis, while XRD considers a more extensive sample area of 5 mm × 5 mm. The SAED pattern of 250 ℃-OA (Fig. 5(e)) shows the spot pattern for Al_3V intermetallic indicated by red arrow and text, while the Al ring pattern is shown by yellow arrow and text.

The size and distribution of precipitates are shown in Fig. 6(a–d) and values are reported in Table 2. The precipitates exhibited nearly spherical geometry with an average size below 7 nm and were observed within the grains as well as grain boundaries. According to Fig. 6(e), coherent precipitate formation within the matrix lattice was observed, indicating no

net alteration in the atomic arrangement. The size and volume fraction of precipitate is displayed in Table 2. The Image J software was implemented to calibrate the image scale and calculate the accurate precipitate size individually. A set of 150–200 precipitates were measured for quantitative analysis. The volume fraction (*f*) of the precipitate was calculated by assuming the precipitate to have a perfectly spherical shape and was determined using the equation:

$$f(\%) = \frac{N(\frac{4}{3}\pi r^3)}{V} \times 100 \quad (2)$$

where *V* is the volume of the analyzed matrix region, *N* is the number of precipitates within that region, and *r* is the average radius of the precipitate. The thickness of the TEM specimens was measured using the energy-filtered transmission electron microscopy (EFTEM) technique. The average TEM specimen thickness was 60 nm. Alloys 150 ℃-PA and 150 ℃-OA exhibited precipitate sizes of 2.4 ± 0.4 and 5.0 ± 1.2 nm, respectively. The volume fraction of precipitate was higher in 150 ℃-PA than in the OA condition. Moreover, the coarsening of the precipitates in the OA condition increased the spacing between precipitates. The precipitate size of 5 nm observed in 150 ℃-OA occurred after 14 days, implying that the precipitate coarsening was not significant. Alloys aged at 250 ℃-PA and 250 ℃-OA showed precipitate sizes of 2.5 ± 0.5 and 3.1 ± 1.9 nm, respectively. The volume fraction of precipitate at 250 ℃ increased from PA to OA condition. Meanwhile, the volume fraction in 250 ℃-PA is lower than 150 ℃-PA. Interestingly, the XRD did not show the precipitate peak at 150 ℃-OA. Given the estimated volume fraction of precipitate within microstructure, it can be possibly deduced that the formation of precipitate at 150 ℃-OA could be below the detection limit of XRD. Additionally, Fig. 4(a) shows lower solid solubility of V in Al at 150 ℃-OA even though the volume fraction of precipitates is lower compared to 150 ℃-PA which indicates a higher mole fraction of the precipitates in 150 ℃-

OA. However, the precipitates for 150 ℃-OA were coarser which could be attributed to the lower volume fraction of the precipitates. This phenomenon is similar to that observed in age-hardening commercial Al alloys where the solubility of the alloying elements decreases with aging time albeit OA alloys may have a lower volume fraction of precipitates than those in PA conditions [3]. It should be noted that the volume fraction of the precipitates measured within the grains depends on the mole fraction of the precipitates formed, spatial distribution, and size.

3.4. Contribution from various strengthening mechanisms

Fig. 7 shows the contribution of the individual strengthening mechanism to the overall yield strength of Al-5at.%V alloy for different age-hardening conditions.

The contribution of grain refinement to strength (σ_{GB}) was estimated using the Hall–Petch relation [42]:

$$\sigma_{\mathrm{GB}} \approx \frac{k}{\sqrt{d}} \quad (3)$$

where d is the grain size (obtained from S/TEM data) and k is the Hall–Petch coefficient (i.e., k = 0.122 MPa $m^{1/2}$ [43]). Fine grains in base alloy offered the highest contribution of 714 MPa. After the aging, the PA condition of all the aging temperatures does not show significant grain growth, and the grain boundary strength does not vary much from the base alloy (Fig. 7). Grain boundary contribution to strength is reduced at OA conditions for all aging temperatures. A significant decrease in hardness was observed for 250 ℃-OA (467 MPa) due to noticeable grain growth from 29 nm to 68 nm.

The increase in yield strength due to solid solution strengthening (σ_{SS}) can be expressed using the equation [43]:

$$\sigma_{SS} = Hc^{\alpha} \quad (4)$$

where H and α are constants while c is the solute concentration present in solid solution denoted by at.%. The values of H and α are reported to be 68 MPa/at.% and 1, respectively [43]. The value of c is obtained using XRD data, as shown in Fig. 4(a). The solid solution contribution in Al-5at.%V base alloy reached up to 211 MPa. The alloy that underwent the aging process showed lower σ_{SS} due to the loss of solid solution, where the 250 ℃-OA condition acquired the least (Fig. 7).

The Orowan strengthening (σ_{Or}) contribution arising from the formation of precipitates can be approximated using the equation [44]:

$$\sigma_{Or} = \sqrt{3}\left[\frac{Gb\ln\delta}{2\pi\delta}\left(\frac{\ln 2r}{\ln\delta}\right)^{3/2}\right] \quad (5)$$

where G is the shear modulus (26 GPa for Al), b is the Burgers vector whose value can be found by $\sqrt{2}/2a$ (here, a = lattice parameter), and δ is the average distance between precipitates. Table 2 shows the values of several parameters used to calculate various strengthening mechanisms. At 150 ℃, the σ_{Or} for the PA condition exhibited a higher value than OA due to small-sized precipitates covering a large volume fraction. On the contrary, at 250 ℃, the OA condition exhibited a high-volume density of precipitates yielding higher σ_{Or} compared to PA. Additionally, the Orowan strengthening contribution is higher in 250 ℃-OA due to finer precipitates and high-volume fraction compared to 150 ℃-OA. Meanwhile, the overall strength in 250 ℃-OA reduced due to the combined effect of grain growth and loss in solid solubility, which is 66% grain growth and 30% V loss from solid solution, respectively, compared to 150 ℃-OA. The effect of grain growth on hardness dominates over the effect of the precipitation. Therefore, the overall strength has dropped in 250 ℃-OA even

when it is exhibiting a high volume fraction of fine precipitates. Owing to the nanocrystalline structure and far-from-equilibrium solid solubility of V, the matrix possesses a high driving force for grain and decomposition of solid solution.

The overall strength of 150 ℃-PA exhibited the highest value due to the optimum contribution achieved from grain refinement, solid solution, and precipitation hardening. A decrease in hardness in over-aged conditions was not only due to the precipitate coarsening but also due to the synergic impact of grain growth and decline in solid solubility. Contemplating the optimum property achieved for 150 ℃-PA, the contribution from grain boundary strengthening provided 59% of the overall strength. In comparison, solid solution strengthening and precipitation strengthening yielded 16% and 25%, respectively. Therefore, grain size plays a vital role in the overall strength, making it dominant among other strengthening contributions in nanocrystalline materials.

3.5. Corrosion behavior

The representative potentiodynamic polarization curves of Al-5at.%V alloy for different aging temperatures and pure Al are presented in Fig. 8. Pure Al is known to be highly corrosion resistant among commercial Al alloys and therefore used here for comparison. The Tafel fit was used to estimate the average corrosion potential (E_{corr}) and corrosion current density (i_{corr}), which are presented along with the average pitting potential (E_{pit}) in Table 3. Base alloy exhibited more noble E_{corr} compared to all other aging conditions. The E_{corr} gradually decreased with aging temperature and time due to the increase in anodic reaction, which was the effect of loss in solid solution and increased precipitation. Section S2 provided in the supplementary file shows the dependency of E_{corr} on precipitate size and solid solubility of V in the matrix. The least E_{corr} was observed in 250 ℃-OA due to precipitation that would lead to the galvanic interaction between the precipitates and matrix. The i_{corr} for over-aged alloys was higher for all aging temperatures. The increase in i_{corr} and shift of E_{corr}

to more negative values for OA conditions were due to an increase in anodic current density. Meanwhile, the E_{pit} was almost similar in the base, 150 ℃-PA, 150 ℃-OA, and 250 ℃-PA alloys. The E_{pit} of 250 ℃-OA decreased significantly compared to all other aging conditions. Nevertheless, the E_{pit} of the base alloy and all age-hardened Al-5at.%V alloys was considerably higher than pure Al, which shows high pitting corrosion resistance of the Al-5V alloy in all the aging conditions.

Fig. 9(a, b) shows the passive film formed on the base and 150 ℃-PA specimens. These specimens were polished and then stored in the glove box for 24 h before preparing samples for the S/TEM analysis. Therefore, these surface films are termed air-borne passive films. The thicknesses of these films were 5.6 and 7.2 nm for the base and 150 ℃-PA specimens, respectively. Compared to the matrix beneath the films, where clear lattice fringes were observed over the grains, the passive film exhibited an amorphous structure. EDS area maps showing the passive film composition and underlying substrate for base alloy are presented in Fig. 9(c), which reveals the enrichment of V at the film/metal interface. Similar behavior was observed for 150 ℃-PA specimen (Fig. S3).

The phenomena of pit initiation and subsequent inhibition of the pit growth from solute interaction are demonstrated by compiling the events from two different specimens as shown in Fig. 10, i.e., 1) 150 ℃-PA air-borne surface—showing secondary phase (i.e., C-rich phase) embedded with matrix, and 2) 250 ℃-PA surface after the immersion in 0.1 M NaCl solution for two hours—illustrating the pitting corrosion induced by C-rich phase. Fig. 10(a) shows the region where the C-rich phase is exposed on the surface before the immersion. The surface film over the C-rich phase was uneven and thin compared to the film over the matrix. Note that the enrichment of V is absent over the C-rich phase, signifying a heterogeneous surface film. Fig. 10(b, c) shows the condition after the immersion in NaCl solution, which illustrates the galvanic corrosion in the matrix around the C-rich phase. Fig. 10(b) depicts the

presence of oxygen at the C-rich phase/matrix interface and at the top-center of the phase, indicating the local oxidation/dissolution of Al. The C-rich phase is cathodic compared to Al [27], which generates significant electrochemical potential differences with the surrounding matrix. Therefore, this site promotes a catalytic effect by providing cathodic activity needed for corroding the matrix and generating hydroxyl ions from the oxygen reduction reaction. Both these factors cause dissolution at the C-rich phase/matrix interface and promote pitting corrosion [45]. Fig. 10(c) exhibits the final state where a pit is formed along the C-rich phase. The EDS map reveals a high amount of O and V surrounding the pit. Higher V content demonstrates obstruction of pit growth by covering the C-rich phase, which decreases the cathodic activity of the C-rich phase. Additionally, V enrichment at the electrolyte/alloy interface is also attributed to retard dissolution of the alloy. Both the factors—decrease in cathodic efficiency of the C-rich phase and decrease in the dissolution of the alloy within pit promotes repassivation in the early stage of pitting corrosion.

4. Discussion

4.1. Passive film and corrosion mechanism

Post corrosion characterization using S/TEM analysis aided in developing an in-depth understanding of the corrosion mechanisms. The solute enrichment discovered at the film/metal interface in Fig. 9(c) is attributed to the higher dissolution kinetics of Al compared to V since the Gibbs free energy for the formation of Al oxide is lower than that for V oxide [46]. The solute-rich region at the interface has shown the potential to increase the stability of the passive film, inhibit the pit propagation when the passive film is compromised, and facilitate repassivation. Solute enrichment can play a role in two ways: 1) by offering an additional oxidized solute barrier layer that lowers dissolution of the pit and therefore repassivate the pit at an early stage, and 2) the ability of the alloy to release solute-based oxyanion within pit during the dissolution, which can deposit on C-rich phase, decrease the

cathodic reaction and cease further pit growth [30,38]. The passive film characterization through XPS shown in our previous work [38] exhibited the presence of oxidized V species (i.e., V^{n+} (n = 3, 4, 5)) in the passive film. With the increase of immersion time in 0.1 M NaCl solution, the V^{5+} species reduced to V^{4+} and V^{3+}, showing the active participation of oxidized V species in the reduction reaction. Vanadium-based oxyanions, also termed vanadate, have been an excellent corrosion inhibitor to Al alloys [47–49] and impede the dissolution kinetics of Al at the corroding region since the oxygen reduction reaction is hindered.

The phenomenon of galvanic interaction between the C-rich phase and matrix reported in this study is an excellent example showing the repassivation tendency of matrix by suppressing the deleterious influence of cathodic phase and is illustrated schematically in Fig. 10(d). During the initial process, the C-rich phase having higher potential promotes oxygen reduction reaction, which induces the matrix to undergo selective dissolution of Al at their interface. Later, the pitting corrosion occurs as the hydrolysis of Al cation decreases the pH at that region by promoting the transportation of Cl^- ion towards it to maintain charge neutrality. These events lead to the formation of an aggressive acidic solution within the pit [50]. Consequently, depending upon the sustainability of acidic solution and kinetics of dissolution within the pit, either the pit can further grow and become stable or cease to grow if the matrix tends to repassivate. In the present case, as the selective dissolution of Al continues, the pit vicinity gets enriched by V coming from solid solution that gradually helps to decrease the dissolution rate, leading to the inability to sustain an aggressive acidic environment within the pit. Additionally, dissolution of V forms vanadate within the pit that deposits on the C-rich phase and suppresses the cathodic reaction. These two events—deposition of V ions in the C-rich phase and slower dissolution within the pit cause repassivation at the early stages of corrosion, which leads to significant improvement in corrosion resistance.

4.2. Grain refinement mechanism, precipitation morphology, and solid solution effect

The supersaturated nanocrystalline alloys are not in the equilibrium state, which offers them with high driving force for decomposition. At the same time, the kinetics of decomposition would depend on properties of the solute element and aging temperature—the higher the temperature, the faster the decomposition. With exposure to elevated temperature, grain growth can be controlled by two primary mechanisms [51]. First is the kinetic mechanism in which grain boundary mobility is restricted by pinning action such as porosity drag, chemical ordering [52], second phase drag [53], and solute drag [54]. For instance, Tellkamp et al. [55] reported the thermal stability of nanocrystalline commercial AA5083 and Al-7.5% Mg produced via cryomilling and consolidated by hipping and extrusion. A large number of precipitates such as Mg_2Si, Al_3Mg_2, and compounds AlN and Al_2O_3 were formed, which retarded grain growth via Zener pinning. Second is the thermodynamic mechanism in which the grain boundary energy is reduced by solute segregation [56, 57]. It is known that the driving force of grain growth increases with the grain boundary energy. Since the segregation of solute atoms at the grain boundaries will affect the grain boundary energy, the grain growth can be minimized by lowering the grain boundary energy. In this work, no solute segregation was observed at grain boundaries. The formation of Al_3V precipitate confirmed here indicates that the grain growth stability could be attributed to Zener pinning, which is consistent with Refs. [58, 59].

The supersaturated nanocrystalline alloy in this work shows the formation of coherent spherical precipitates in Fig. 6(e), indicating no alteration to the atomic arrangement. The surface energy and lattice strain govern the morphology of the precipitates. The coherent precipitates tend to be spherical as the lattice strain energy is low, and a spherical shape lowers the surface area and, therefore, lowers net surface energy. Precipitate formation and growth are controlled by the diffusion coefficient of solute [60]. The diffusion coefficient of

V in Al is low (4.85×10^{-24} m^2/s at 400 °C [26]), which has contributed to slower nucleation and growth of the precipitates in this alloy. The solid solution strengthening comes from the enhanced solid solubility of V in the Al matrix, which has modified the lattice parameter of the alloy as shown in Table 2. Introducing the substitutional solute into the pool of matrix atoms affects the atomic arrangement. The change in lattice parameter depends upon the solid solubility and the size of solute atom and was discussed in our previous work [16]. The contraction of the lattice parameter demonstrates the decrease in the interatomic spacing, which causes lattice mismatch and influences the bonding between the atoms. Further investigation is required to model the atomic arrangement due to modification in lattice parameters and will be the scope for future work using density functional theory (DFT).

4.3. Influence of precipitate on corrosion resistance

The supersaturated nanocrystalline Al-5at.%V alloy excellently responded to precipitation hardening. The strength of the alloy was enhanced at peak-aged condition. Additionally, the corrosion performance was retained at the PA condition with an insignificant decline in E_{corr} and i_{corr} compared to the base alloy that directs to the loss in solid solution to form precipitates. Literatures have also shown that the corrosion performance of an alloy can be preserved if the size and density of the precipitates are below certain critical range [44, 61–63]. For instance, the 7xxx series Al alloys have shown lower susceptibility to pitting corrosion as the size of η phase was below 5 nm [63], while others reported the size of S phase below 3 nm in the Al-Cu-Mg alloy [61]. Comparably, in this work, the peak-aged condition of 150 and 250 °C aging temperatures having the precipitate size below around 3 nm showed similar corrosion performance as base alloy, indicating that the precipitate size is below the critical range. Whereas over-aged conditions of 150 and 250 °C having the precipitate size above the critical range of 3 nm have shown deterioration in corrosion resistance. Additionally, aging the alloy at an elevated temperature can cause various

modifications to the microstructure. Since the microstructure consists of nanocrystalline supersaturated solid solution, it contains high driving force for decomposition. Most of the time, the decomposition can play a detrimental role in corrosion performance, but it may also locally favor the properties, which raises complication in understanding the overall scenario. For instance, the surface shows a passive film growth after aging compared to base alloy, which could result in additional barriers during corrosion. The growth of passive film in Al alloy is one of the factors that govern to influence corrosion resistance. The film growth is possibly favoring to reduce the corrosion current density up to a certain period as seen in PA condition (Table 3), after which the corrosion rate is observed to spike up as severe decomposition occurs. Additionally, the effect of precipitates on galvanic corrosion depends upon the size, distribution, and number of the precipitates. Significant difference in corrosion behavior of 250 ℃-OA and base alloy is observed which could be attributed to the substantial loss in solid solubility and volume fraction of precipitates exceeding a critical value. It should be noted that V content in the matrix (solid solubility) is playing a critical role.

An example of heterogeneous microstructure showing high corrosion resistance is presented, which demonstrates the importance of microstructure on corrosion performance. The deleterious influence of precipitates and cathodic particles can be suppressed by choosing the appropriate composition and microstructure. Moreover, the application of S/TEM in characterizing the surface film and understanding the corrosion mechanisms is presented. Surface film characterization has been reported mainly by X-ray photoelectron spectroscopy and secondary ion mass spectrometry, which lacks lateral resolution and therefore limits their application in studying the surface films on heterogeneous microstructure. The use of S/TEM in studying the surface film and corrosion presented herein should facilitate the application of this state-of-the-art technique in investigating atomic-scale

corrosion phenomena and open up new possibilities in designing high-strength and corrosion-resistant alloys.

5. Conclusions

The age-hardening behavior and corrosion mechanisms in nanocrystalline Al-V supersaturated solid solution produced by high-energy ball milling have been investigated. The role of composition and microstructure in developing alloys with properties exceeding the conventional limits has been elucidated. Application of the S/TEM in characterizing the surface film and understanding corrosion mechanisms provided a visual demonstration. The main conclusions can be listed as follows:

(1) Al-5at.%V alloy with high solid solubility of V—far from equilibrium solubility and grain size below 100 nm was produced by high-energy ball milling. The alloy exhibited high corrosion resistance and hardness attributed to the combined influence of high solid solubility of V and nanocrystalline structure.

(2) The alloy responded to age-hardening that was performed at three temperatures—150, 200, and 250 °C. Age-hardening kinetics increased with increasing temperature. The 150 °C-PA led to optimum conditions for hardness and corrosion resistance. The contributions from grain refinement, precipitation hardening, and solid solution strengthening were considered. Grain refinement had the most substantial influence on the strength, whereas solid solubility of the V in Al played a major role in determining the corrosion resistance. The high solid solubility of the V was deemed essential for high corrosion resistance and negating the deleterious influence of the microstructural heterogeneities.

(3) The corrosion phenomena studied using S/TEM visually demonstrated: i) solute (V) enrichment at the film/metal interface that provided an additional barrier to passive film, ii)

thin and uneven passive film at the cathodic C-rich phase, iii) localized corrosion due to the cathodic C-rich phases, and iv) the deposition of solute over C-rich phase, which suppressed the cathodic efficiency and caused repassivation in early stages of corrosion.

Acknowledgments

The authors would like to acknowledge the financial support received from the National Science Foundation (Nos. NSF-CMMI 1760204 and NSF-CMMI 2131440) under the direction of Dr. Alexis Lewis. This work was performed in part at the Analytical Instrumentation Facility (AIF) at North Carolina State University, supported by the State of North Carolina and the National Science Foundation (award number ECCS-2025064). The AIF is a member of the North Carolina Research Triangle Nanotechnology Network (RTNN), a site in the National Nanotechnology Coordinated Infrastructure (NNCI).

References

[1] L. Stemper, M.A. Tunes, P. Oberhauser, P.J. Uggowitzer, S. Pogatscher, Acta Mater. 195 (2020) 541–554.

[2] A. Mohammadi, N.A. Enikeev, M.Y. Murashkin, M. Arita, K. Edalati, Acta Mater. 203 (2021) 116503.

[3] I.J. Polmear, Light Alloys, Butterworth-Heinemann, Oxford, 2005.

[4] R.K. Gupta, B.S. Murty, N. Birbilis, An Overview of High-Energy Ball Milled Nanocrystalline Aluminum Alloys, Springer, Berlin, 2017. pp.1–99.

[5] J.G. Kaufman, Introduction to Aluminium Alloys and Tempers, ASM International, Flevoland, 2000. pp.87–118.

[6] Z. Zhao, G.S. Frankel, Corrosion Sci. 49 (2007) 3064–3088.

[7] M.K. Cavanaugh, J.C. Li, N. Birbilis, R.G. Buchheit, J. Electrochem. Soc. 161 (2014) C535–C543.

[8] J. Li, N. Birbilis, R.G. Buchheit, Corrosion Sci. 101 (2015) 155–164.

[9] J. Christudasjustus, C.S. Witharamage, G. Walunj, T. Borkar, R.K. Gupta, J. Mater. Sci. Technol. 122 (2022) 68–76.

[10] J. Esquivel, H.A. Murdoch, K.A. Darling, R.K. Gupta, Mater. Res. Lett. 6 (2018) 79–83.

[11] K.M. Youssef, R.O. Scattergood, K.L. Murty, C.C. Koch, Scr. Mater. 54 (2006) 251–256.

[12] L. Esteves, C.S.S. Witharamage, J. Christudasjustus, G. Walunj, S.P.P. O'Brien, S. Ryu, T. Borkar, R.E.E. Akans, R.K.K. Gupta, J. Alloy. Compd. 857 (2021) 158268.

[13] L. Esteves, J. Christudasjustus, S.P. O'Brien, C.S. Witharamage, A.A. Darwish, G. Walunj, P. Stack, T. Borkar, R.E. Akans, R.K. Gupta, Corrosion Sci. 186 (2021) 109465.

[14] R.K. Gupta, D. Fabijanic, R. Zhang, N. Birbilis, Corrosion Sci. 98 (2015) 643–650.

[15] H. Miyamoto, Mater. Trans. 57 (2016) 559–572.

[16] J. Christudasjustus, T. Larimian, J. Esquivel, S. Gupta, A.A. Darwish, T. Borkar, R.K. Gupta, Mater. Lett. 320 (2022) 132292.

[17] G.J. Fan, W.N. Gao, M.X. Quan, Z.Q. Hu, Mater. Lett. 23 (1995) 33–37.

[18] J. Esquivel, M.G. Wachowiak, S.P. O'Brien, R.K. Gupta, J. Alloy. Compd. 744 (2018) 651–657.

[19] Q. Luo, H.C. Chen, W. Chen, C.C. Wang, W. Xu, Q. Li, Scr. Mater. 187 (2020) 413–417.

[20] Q. Luo, Y.L. Guo, B. Liu, Y.J. Feng, J.Y. Zhang, Q. Li, K. Chou, J. Mater. Sci. Technol. 44 (2020) 171–190.

[21] Y. Li, Y. Jiang, B. Hu, Q. Li, Scr. Mater. 187 (2020) 262–267.

[22] Y. Li, Y. Jiang, B. Liu, Q. Luo, B. Hu, Q. Li, J. Mater. Sci. Technol. 65 (2021) 190–201.

[23] Y. Li, B. Hu, Q.F. Gu, B. Liu, Q. Li, Scr. Mater. 160 (2019) 75–80.

[24] V.B. Vukkum, J. Christudasjustus, A.A. Darwish, S.M. Storck, R.K. Gupta, NPJ Mater. Degrad. 6 (2022) 2.

[25] C.S. Witharamage, J. Christudasjustus, R.K. Gupta, J. Mater. Eng. Perform. 30 (2021) 3144–3158.

[26] K.E. Knipling, D.C. Dunand, D.N. Seidman, Int. J. Mater. Res. 97 (2006) 246–265.

[27] E. Mccafferty, Introduction to Corrosion Science, Springer, New York, 2009.

[28] M. Metikoš-Hukovi, N. Radi, Z. Grubač, H.A. Tonejcv, Electrochim. Acta 47 (2002) 2387–2397.

[29] E.L. Principe, B.A. Shaw, G.D. Davis, Corrosion 59 (2003) 295–313.

[30] G.D. Davis, B.A. Shaw, B.J. Rees, M. Ferry, J. Electrochem. Soc. 140 (1993) 951–959.

[31] B.A. Shaw, G.D. Davis, T.L. Fritz, B.J. Rees, W.C. Moshier, J. Electrochem. Soc. 138 (1991) 3288–3295.

[32] W.C. Moshier, J. Electrochem. Soc. 134 (1987) 2677.

[33] G.S. Frankel, R.C. Newman, C.V. Jahnes, M.A. Russak, J. Electrochem. Soc. 140 (1993) 2192–2197.

[34] G.S. Frankel, X.B. Chen, R.K. Gupta, S. Kandasamy, N. Birbilis, J. Electrochem. Soc. 161 (2014) C195–C200.

[35] J. Esquivel, R.K. Gupta, J. Electrochem. Soc. 167 (2020) 081504.

[36] A. Kosari, H. Zandbergen, F. Tichelaar, P. Visser, H. Terryn, J.M.C. Mol, Corrosion Sci. 192 (2021) 109864.

[37] D.R. Baer, J.E. Amonette, M.H. Engelhard, D.J. Gaspar, A.S. Karakoti, S. Kuchibhatla, P. Nachimuthu, J.T. Nurmi, Y. Qiang, V. Sarathy, S. Seal, A. Sharma, P.G. Tratnyek, C.M. Wang, Surf. Interface Anal. 40 (2008) 529–537.

[38] C.S. Witharamage, J. Christudasjustus, J. Smith, W. Gao, R.K. Gupta, NPJ Mater. Degrad. 6 (2022) 1–9.

[39] R.W.G. Wyckoff, Cryst. Struct. 1 (1963) 7–83.

[40] J.L. Murray, Bull. Alloy Phase Diagrams 10 (1989) 351–357.

[41] A.L. Patterson, Phys. Rev. 56 (1939) 978–982.

[42] Z.C. Cordero, B.E. Knight, C.A. Schuh, Int. Mater. Rev. 61 (2016) 495–512.

[43] J. Esquivel, R.K. Gupta, J. Alloy. Compd. 760 (2018) 63–70.

[44] R.K. Gupta, D. Fabijanic, T. Dorin, Y. Qiu, J.T. Wang, N. Birbilis, Mater. Des. 84 (2015) 270–276.

[45] G.O. Ilevbare, O. Schneider, R.G. Kelly, J.R. Scully, J. Electrochem. Soc. 151 (2004) B453–B464.

[46] H. Habazaki, K. Shimizu, P. Skeldon, G.E. Thompson, G.C. Wood, X. Zhou, Trans. Inst. Metal Finish. 75 (1997) 18–23.

[47] R.L. Cook, S.R. Taylor, Corrosion 56 (2000) 321–333.

[48] M. Iannuzzi, G.S. Frankel, Corrosion Sci. 49 (2007) 2371–2391.

[49] M. Iannuzzi, T. Young, G.S. Frankel, J. Electrochem. Soc. 153 (2006) B533–B541.

[50] G.S. Frankel, J. Electrochem. Soc. 145 (1998) 2186–2198.

[51] C.C. Koch, J. Mater. Sci. 42 (2007) 1403–1414.

[52] C. Bansal, Z.Q. Gao, B. Fultz, Nanostruct. Mater. 5 (1995) 327–336.

[53] K. Boylan, D. Ostrander, U. Erb, G. Palumbo, K.T. Aust, Scr. Metal. Mater. 25 (1991) 2711–2716.

[54] A. Michels, C.E. Krill, H. Ehrhardt, R. Birringer, D.T. Wu, Acta Mater. 47 (1999) 2143–2152.

[55] V.L. Tellkamp, A. Melmed, E.J. Lavernia, Metall. Mater. Trans. A 32A (2001) 2335–2343.

[56] R. Kirchheim, Acta Mater. 50 (2002) 413–419.

[57] J. Weissmüller, J. Mater. Res. 9 (1994) 4–7.

[58] Y.C. Chen, M.E. Fine, J.R. Weertman, R.E. Lewis, Scr. Metall. 21 (1987) 1003–1008.

[59] Y.C. Chen, M.E. Fine, J.R. Weertman, Acta Metal. Mater. 38 (1990) 771–780.

[60] R.E. Smallman, A.H.W. Ngan, Modern Physical Metallurgy, Eighth Ed., Butterworth-Heinemann, Oxford, 2013.

[61] K.D. Ralston, N. Birbilis, M. Weyland, C.R. Hutchinson, Acta Mater. 58 (2010) 5941–5948.

[62] K.D. Ralston, N. Birbilis, M.K. Cavanaugh, M. Weyland, B.C. Muddle, R.K.W. Marceau, Electrochim. Acta 55 (2010) 7834–7842.

[63] R.K. Gupta, A. Deschamps, M.K. Cavanaugh, S.P. Lynch, N. Birbilis, J. Electrochem. Soc. 159 (2012) C492–C502.

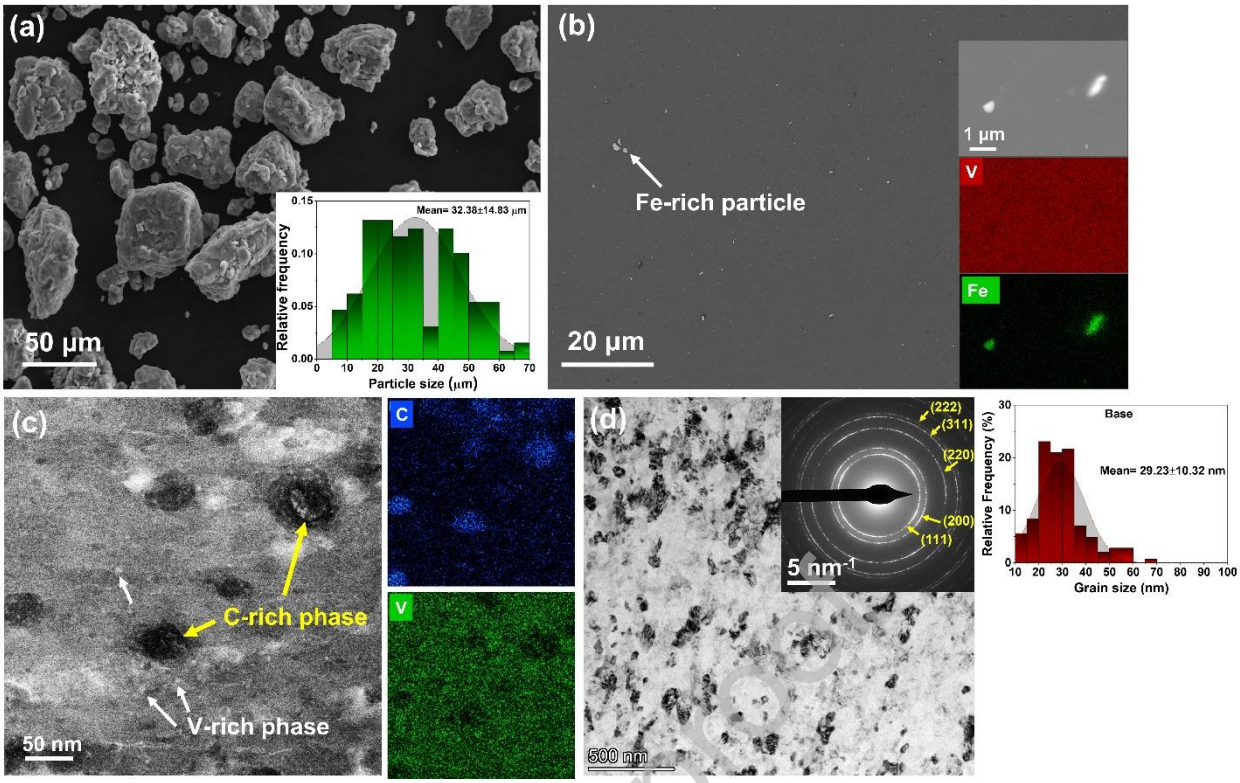

Fig. 1. (a) Backscattered electron image showing Al-5at.%V HEBM powder. Particle size distribution is shown in the inset image; (b) BSE image exhibiting Al-5at.%V base alloy. Inset shows a high magnification image of bright particles and EDS area map, confirming the bright particles to be Fe-rich phase; (c) STEM-HAADF image with EDS maps revealing heterogeneous matrix. The dark phase denoted by yellow arrows is the C-rich phase, the bright phase denoted by white arrows is the V-rich phase, and (d) TEM image with SAED pattern confirming the nanocrystalline grains along with grain size distribution.

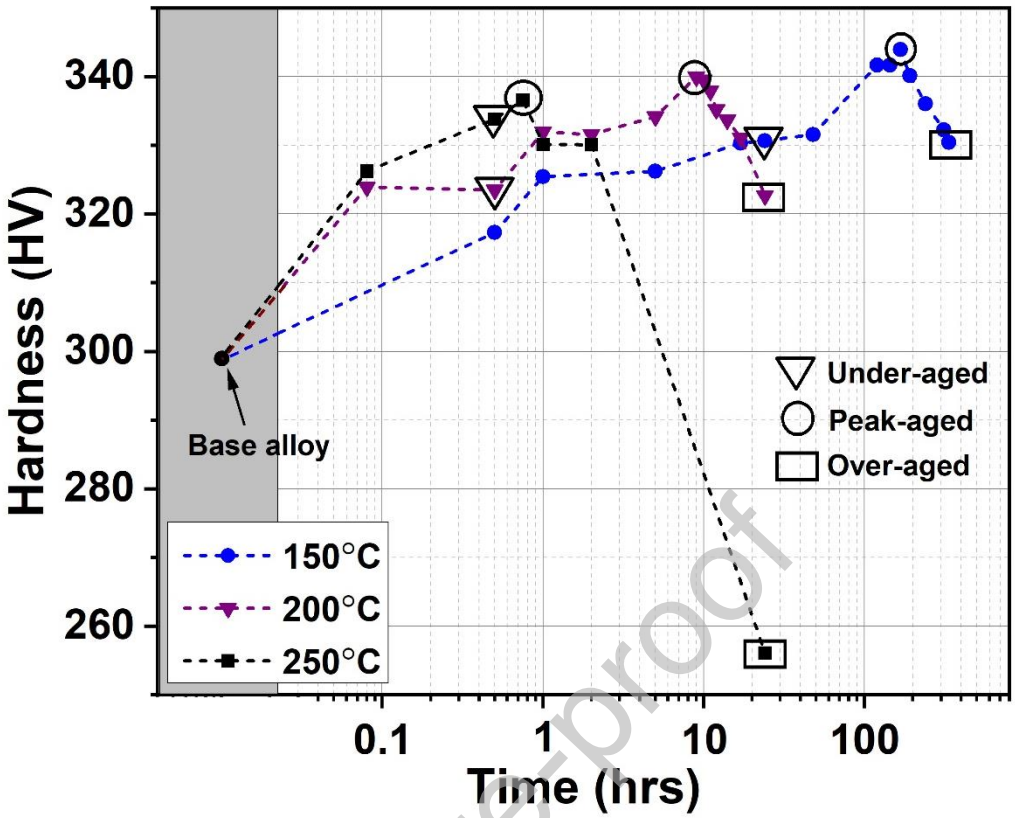

Fig. 2. Vickers hardness as a function of aging time at aging temperatures of 150, 200, and 250 °C. Base alloy is the ball-milled and subsequently cold compacted alloy without any aging. The under-aged, peak-aged, and over-aged conditions selected for in-depth studies are indicated by a triangle, circle, and box, respectively.

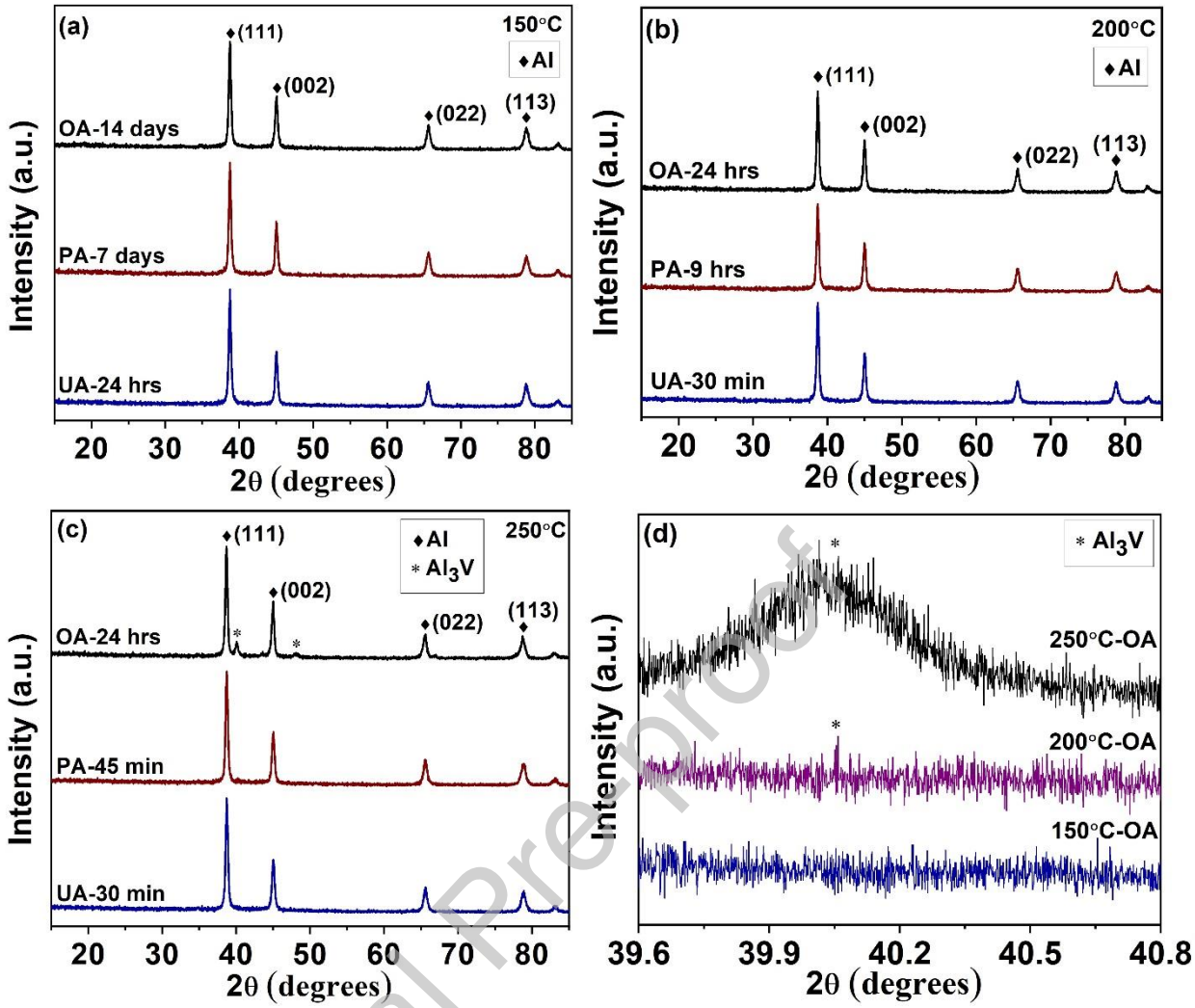

Fig. 3. XRD scans for Al-5at.%V alloy in under-aged (UA), peak-aged (PA), and over-aged (OA) conditions for three aging temperatures (a) 150, (b) 200, and (c) 250 ℃; (d) high-resolution XRD scans of OA alloy after aging at three temperatures to show Al_3V peak. High-resolution XRD scans were performed at a scanning rate of 0.08°/min and step size of 0.0012° between 39.6° and 41°.

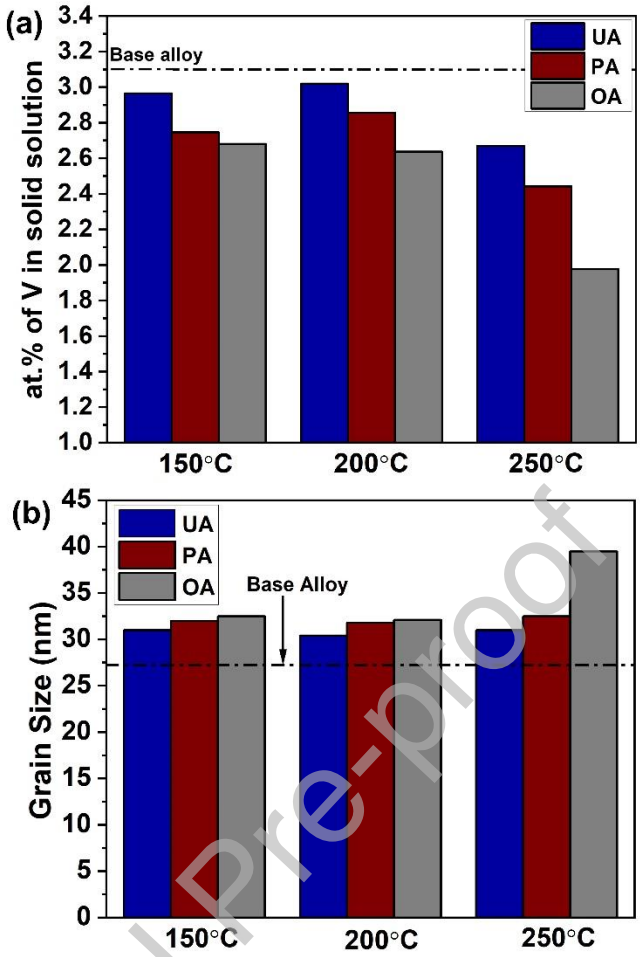

Fig. 4. (a) Solid solubility of V in Al, and (b) grain size for the base, 150, 200, and 250 °C at different aging conditions. Base alloy is the unaged condition. The dotted dash line indicates the base alloy values.

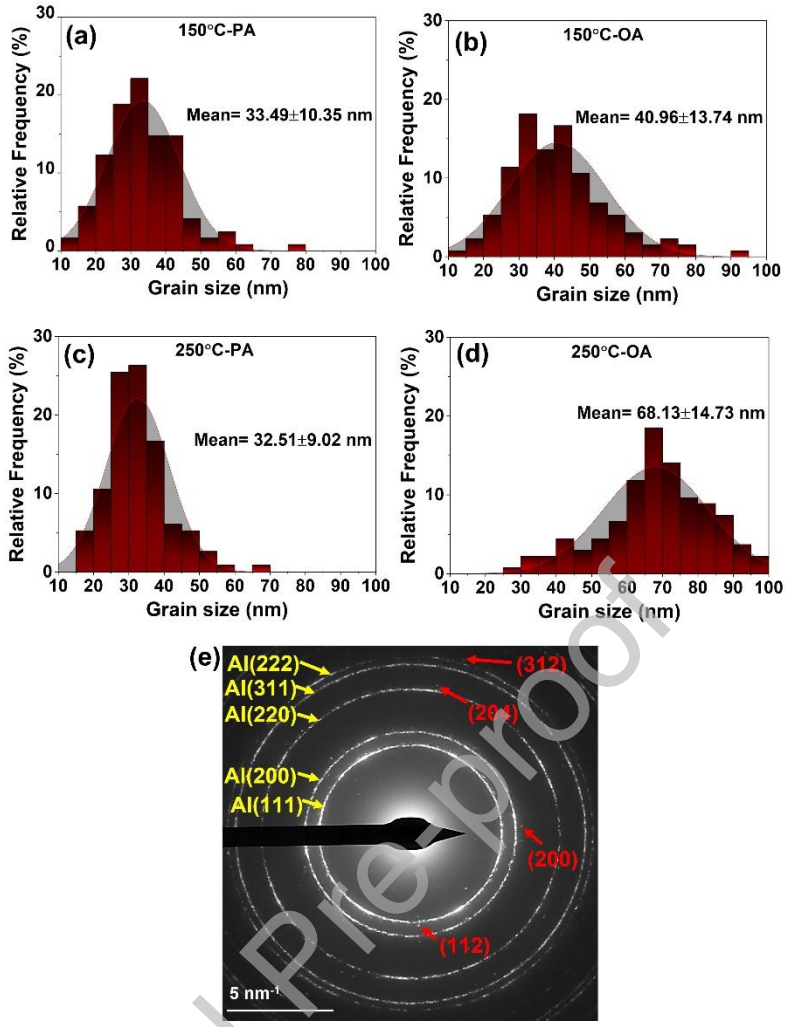

Fig. 5. Grain size distribution graphs estimated using TEM-DF images for (a) 150 ℃-PA, (b) 150 ℃-OA, (c) 250 ℃-PA, and (d) 250 ℃-OA; (e) SAED pattern of 250℃-OA representing the (hkl) planes for Al ring pattern (yellow arrow and text) and Al_3V spot pattern (red arrow and text)

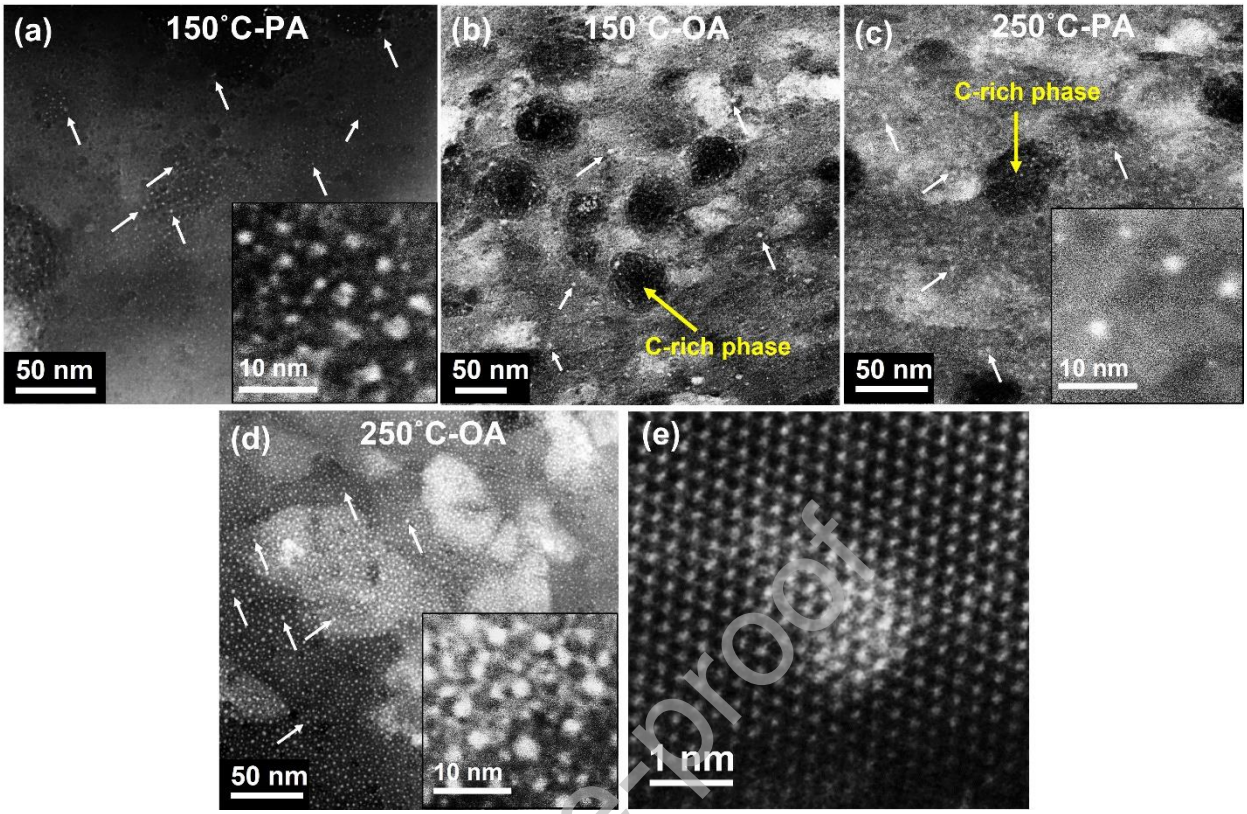

Fig. 6. STEM-DF images showing the size and distribution of precipitates for (a) 150 ℃-PA, (b) 150 ℃-OA, (c) 250 ℃-PA, and (d) 250 ℃-OA conditions. The white arrow indicates the precipitate. High magnification images are provided as insets at the bottom-right corner. The dark phase is C-rich phase introduced through steric acid during milling; (e) high-resolution STEM-HAADF image of a precipitate obtained from 250 ℃-OA, indicating no net alteration in the atomic arrangement within the matrix lattice

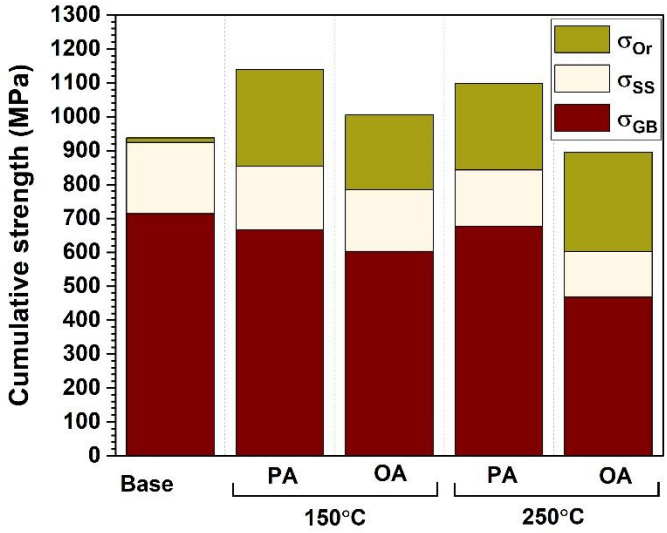

Fig. 7. Graph of estimated overall strength using strengthening contribution from grain boundary (σ_{GB}), solid solution (σ_{SS}), and precipitate hardening (σ_{Or}) in age-hardened Al-5at.%V alloy

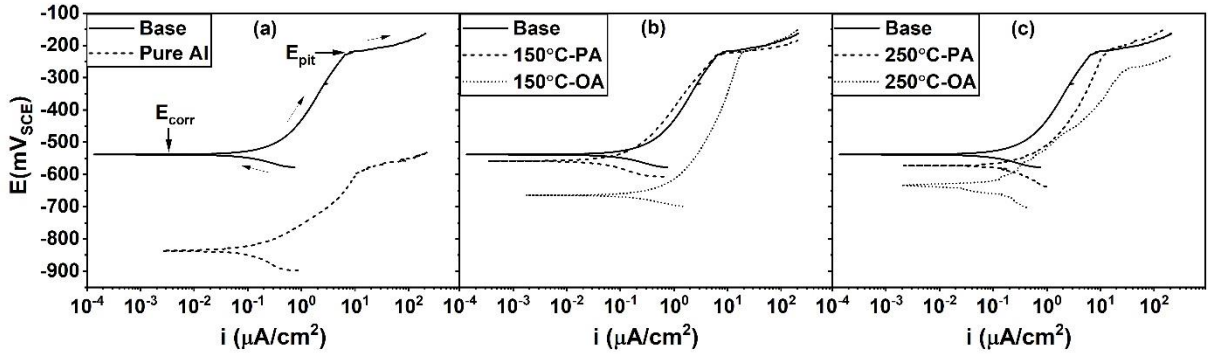

Fig. 8. Representative potentiodynamic polarization curves showing anodic polarization performed in 0.01 M NaCl solution for (a) base and pure Al; age-hardened specimens at (b) 150 ℃, and (c) 250 ℃

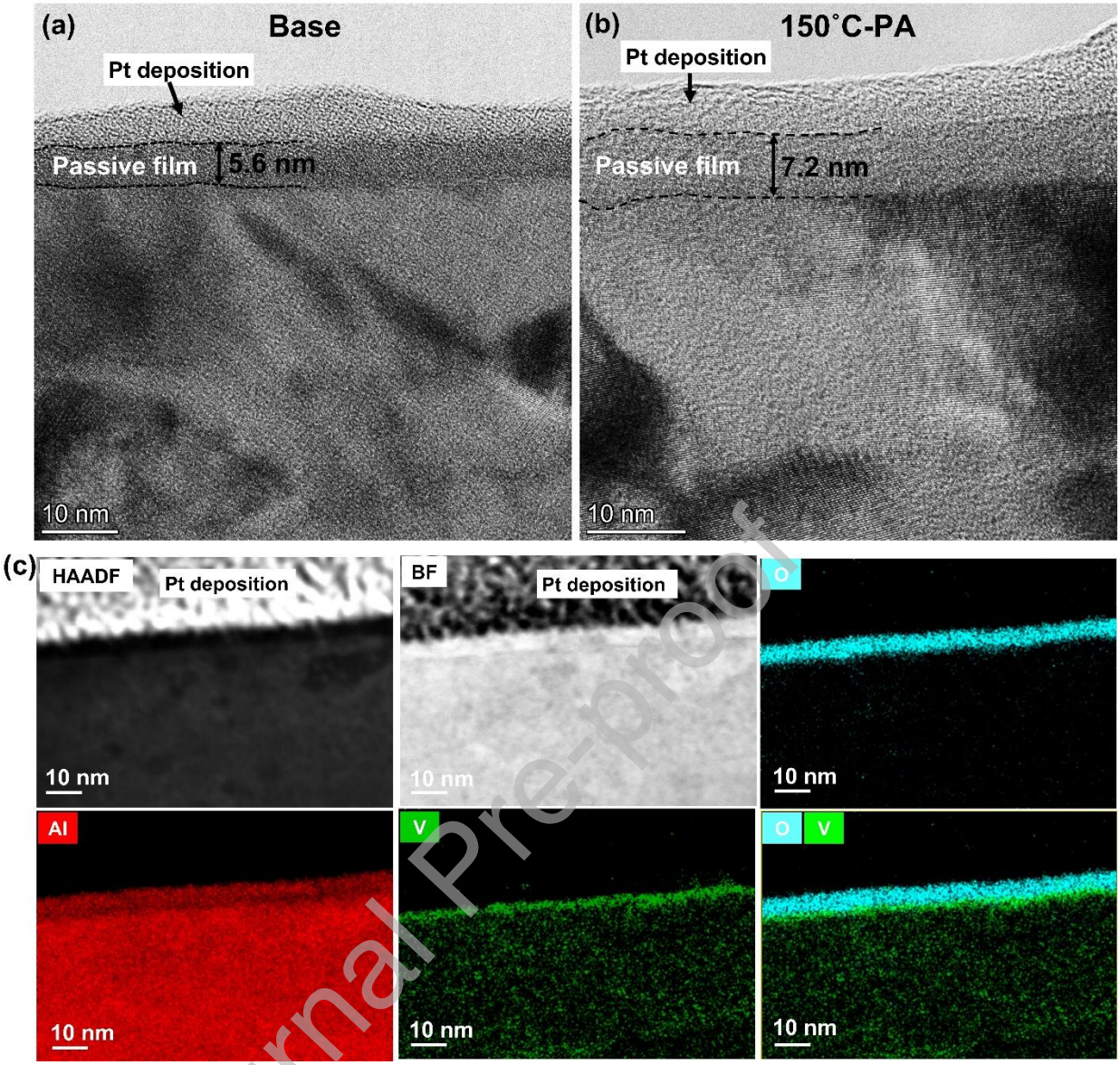

Fig. 9. TEM images showing the air-borne passive film of (a) base and (b) 150 ℃-PA specimens; (c) STEM HAADF and BF image with EDXS mapping of base alloy over the surface and sub-surface region revealing the V enrichment at film/metal interface. The STEM-EDXS mapping of 150 ℃-PA specimens is provided in supplementary data

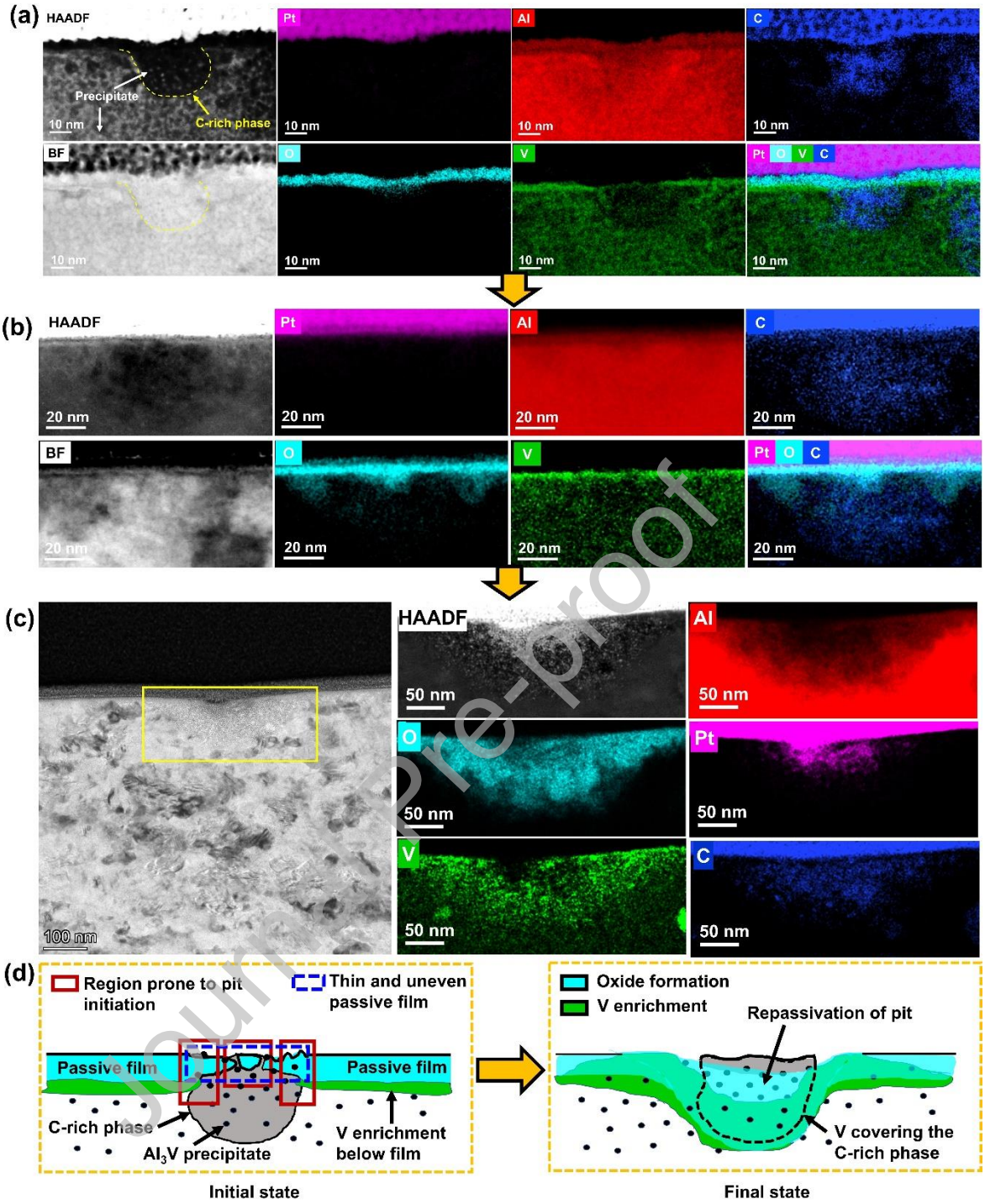

Fig. 10. (a) STEM-EDXS mapping of 150 °C-PA air-borne surface shows the uneven and thin passive film due to the presence of C-rich phase, (b) STEM-EDXS on the surface of 250 °C-PA specimen after the immersion reveals the initiation of galvanic corrosion due to C-rich phase, (c) TEM image exhibiting the pit formation on the surface of 250 °C-PA specimen after the immersion. STEM-EDXS was performed over the yellow box. The O and V enrichment observed in the vicinity of the pit infer to repassivation tendency; (d) schematic diagram shows the initial (air-borne) and final (after 2 hours immersion in NaCl) phenomena corresponding to (a) and (c), respectively. The final state represents the V deposition in C-rich phase that reduces the electrochemical potential difference between that region and matrix.

Table 1 Aging temperature and conditions along with aging time.

Aging temperature (℃)	Notation	Aging duration
150	150 ℃-UA	24 h
	150 ℃-PA	7 d
	150 ℃-OA	14 d
200	200 ℃-UA	30 min
	200 ℃-PA	9 h
	200 ℃-OA	24 h
250	250 ℃-UA	30 min
	250 ℃-PA	45 min
	250 ℃-OA	24 h

Table 2 Values of parameters used in the strengthening contribution calculations.

Aging temperature	Aging condition	Lattice parameter α (Å)	Burgers vector b (nm)	Grain Size (nm)	Precipitate size r (nm)	Particle spacing δ (nm)	f (%)
Base	Unaged	4.0316	0.2851	29.2 ± 10.3	1.6 ± 0.3	27.6	0.07
150 ℃	PA	4.0279	0.2848	33.5 ± 10.4	2.4 ± 0.4	4.7	1.70
	OA	4.0284	0.2849	41.0 ± 13.7	5.0 ± 1.2	12.0	1.13
250 ℃	PA	4.0303	0.2850	32.5 ± 9.0	2.5 ± 0.5	5.4	1.20
	OA	4.0340	0.2852	68.1 ± 14.7	3.1 ± 1.9	5.1	3.12

Table 3 Average electrochemical parameters for age-hardened Al-5at.%V alloys

Aging temperature	Aging condition	E_{corr} (mV_{SCE})	i_{corr} ($\mu A/cm^2$)	E_{pit} (mV_{SCE})
Pure Al	–	–851 ± 44	0.09 ± 0.011	–580 ± 14
Base	Unaged	–534 ± 11	0.08 ± 0.005	–230 ± 4
150 ℃	PA	–561 ± 11	0.054 ± 0.013	–228 ± 2
	OA	–587 ± 83	0.128 ± 0.082	–226 ± 5
250 ℃	PA	–586 ± 17	0.089 ± 0.111	–226 ± 12
	OA	–668 ± 37	0.103 ± 0.017	–298 ± 31

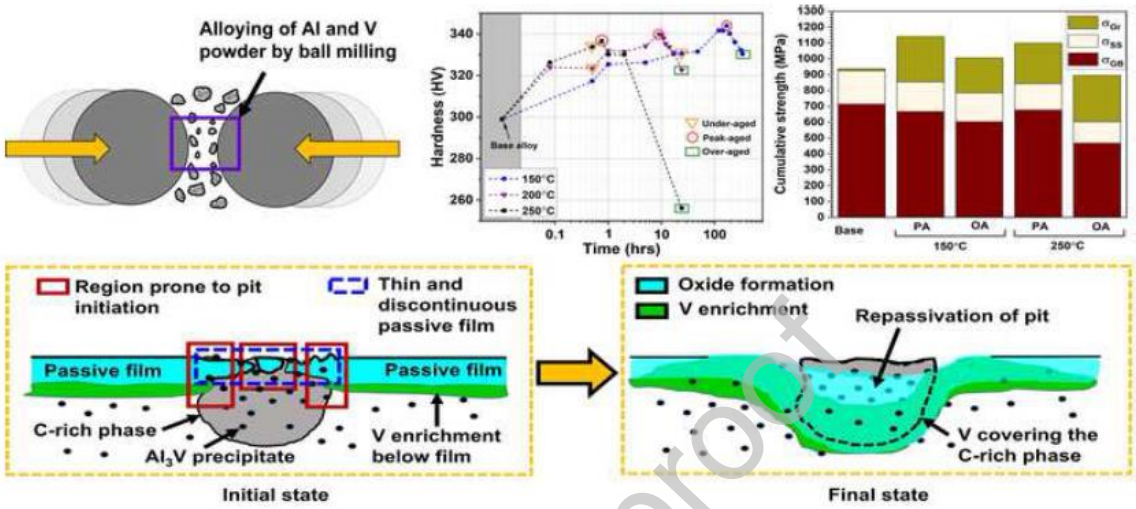

Graphical